ADVANCED MATERIALS
www.advmat.de

Decoding Chemo-Mechanical Failure Mechanisms of Solid-State Lithium Metal Battery Under Low Stack Pressure via Optical Fiber Sensors

Guocheng Li, Taolue Zhang, Jiayue Tang, Mingtao Liu, Yizhan Xie, Jingya Yu, Xiaobin Hui, Canbin Deng, Xibin Lu, Yoonseob Kim, Jiaqiang Huang, and Zheng-Long Xu**

All solid-state lithium (Li) metal batteries (ASSLBs) using ceramic-polymer hybrid solid electrolytes hold the promise for high-performance energy storage application, but they still suffer from the interfacial deterioration and dendritic Li penetration issues, particularly under low stack pressures. Therefore, understanding and mastering the underlying chemo-mechanical failure mechanisms become essential. Herein, the chemo-mechanical evolutions by operando monitoring the amplitude and heterogeneity of interfacial stress through an embedded optical fiber sensor are revealed. It is found that the uneven stripping/deposition of Li metal induces rapid and non-uniform stress growth at the interface, deteriorating interfacial contact with the Li-filament growth. Based on these insights, Li metal is replaced with an architectural lithium-tin anode, which demonstrates uniform stress and improved performance even under low stack pressure. This work not only offers a quantitative way to operando track the uniformity of interfacial stress but also provides critical insights into mastering the chemo-mechanics of ASSLBs.

1. Introduction

The potential safety hazards of Li-ion batteries (LIBs) arisen from intrinsic flammability of organic liquid electrolytes has been recognized as a serious impediment to its further application in consumer electronics and electric vehicles.[1–4] All solid-state lithium (Li) metal batteries (ASSLBs) using nonflammable solid-state electrolytes can intrinsically address the safety issues, and fulfill ever-increasing demands on the high-energy densities by using high-capacity anodes (e.g., Li metal, silicon, and Li_xSi derivatives).[5,6] Li metal has been considered as the holy grail in ASSLBs due to its lowest reduction potential (−3.04 V vs the standard hydrogen electrode) and the highest theoretical specific capacity (3860 mAh g^{-1}) among the potential anodes.[7] However, host-less Li metal suffers uneven electrochemical stripping/plating behaviors and the unstable Li/electrolyte interface during cycling.[8] Recently, the failure of ASSLBs has been closely linked to the chemo-mechanical instability at the interfaces, which is arbitrarily reflected by the increased interfacial ohmic resistance and short circuit.[9] To address the interfacial deterioration, the lab-scale pellet-type cells have been operated under ultrahigh stack pressures (≥100 MPa).[10,11] The abuse of ultrahigh stack pressures is costly

G. Li, J. Yu, X. Hui, Z.-L. Xu
Research Center for Deep Space Explorations
Department of Industrial and Systems Engineering
The Hong Kong Polytechnic University
Hung Hom, Hong Kong SAR 999077, P. R. China
E-mail: zhenglong.xu@polyu.edu.hk

G. Li, T. Zhang, J. Tang, M. Liu, Y. Xie, C. Deng, X. Lu, J. Huang
Sustainable Energy and Environment Thrust and Guangzhou Municipal Key Laboratory of Materials Informatics
The Hong Kong University of Science and Technology (Guangzhou)
Guangdong 511400, P. R. China
E-mail: seejhuang@hkust-gz.edu.cn

The ORCID identification number(s) for the author(s) of this article can be found under https://doi.org/10.1002/adma.202417770

DOI: 10.1002/adma.202417770

G. Li
College of Chemistry and Environmental Engineering
Yangtze University
Jingzhou 434000, P. R. China

C. Deng, X. Lu, J. Huang
Academy of Interdisciplinary Studies
The Hong Kong University of Science and Technology
Clear Water Bay, Kowloon, Hong Kong 999077, P. R. China

Y. Kim
Department of Chemical and Biological Engineering
The Hong Kong University of Science and Technology
Clear Water Bay, Kowloon, Hong Kong SAR 999077, P. R. China

J. Huang
HKUST Shenzhen-Hong Kong Collaborative Innovation Research Institute, Futian
Shenzhen, Guangdong 518045, P. R. China

Z.-L. Xu
Research Institute for Advanced Manufacturing
The Hong Kong Polytechnic University
Hung Hom, Hong Kong SAR 999077, P. R. China

and detrimental to the pressure-driven Li creep behavior.[12] Deciphering and stabilizing the Li/solid-state electrolyte interface at low stack pressures are crucial for approaching viable ASSLBs.

In early studies, the interfacial evolution of ASSLBs was characterized by post-mortem analysis with ex-situ or/and destructive methods, like scanning electron microscopy (SEM) and atomic force microscopy (AFM).[13] These methods fail to reveal the real-time interfacial information under practical working scenarios with uniaxial stack pressures. Recently, increasing efforts have been emphasized on monitoring the interfacial chemistry in ASSLBs with in-situ techniques. For example, the in-situ X-ray computed tomography (XCT) images showed the development of a dendritic crack from initiation through propagation to induce the cracks of sulfide ceramic electrolyte and the completed short circuit under a moderate stack pressure of 7 MPa.[14] The in-situ observation and stress measurement of individual Li whiskers growing from Li_2CO_3 solid electrolyte has also been realized through an AFM with an environmental transmission electron microscope (AFM-TEM) setup.[13] They found that the yield strength of Li whiskers under pure mechanical loading reached as high as 244 MPa, which far exceeded the applied stack pressures on ASSLBs in most works. This work implies the ineffectiveness of simply increasing stack pressures on ASSLBs to mitigate the dendritic Li growth. Despite the informative findings from these cutting-edge tools, the inaccessibility of these expensive instruments and the significant differences between micro-cells for these characterizations and the real batteries make it imperative to explore cost-effective and scalable techniques to visualize the cell failure mechanisms toward rational design of Li metal anodes.

Optical fiber Bragg grating (FBG) sensor has emerged as an effective technique for operando decoding the chemical/thermal events and stress evolutions in rechargeable batteries by leveraging unique virtues of fiber sensors, including the micro-size, anti-corrosion capability and immunity to electromagnetic interferences.[15–18] We have demonstrated the feasibility of embedding FBG sensors into 18650-type commercial Na- and Li-ion cells, and successfully tracked the thermal/chemical events such as the formation and structural evolution of solid electrolyte interphase (SEI).[19] By incorporating the FBG sensors into pouch cells, the stress variation of sulfur cathodes and anode-free Li metal batteries in liquid electrolyte have been precisely monitored.[20,21] More recently, we extended the application of FBG sensors to monitor the stresses driven from Li stripping/plating of Li metal or Li-In composite anodes in Swagelok or modified coin cells with liquid or sulfide ceramic electrolytes.[22] These versatile successes recommend FBG sensors useful in studying ASSLBs at the electrode level, however, quantifying the heterogeneity in addition to the amplitude of stress at electrolyte/electrode interface remains challenging for low-pressure ASSLBs.

In this work, we implement FBG sensors in solid-state batteries for operando monitoring the chemo-mechanical evolutions at electrolyte/electrolyte interface and provide an effective strategy for stable ASSLBs under low stack pressures. By tracking the real-time spectral responses of the implemented FBG sensors inside the solid-state Li||Li Swagelok cells, we quantify the non-uniform stress distribution at the Li/electrolyte interface. The heterogenous stress rapidly accumulated in various dimensions with cycling due to the ever-increasing amount of porous Li metal. The non-uniform and deteriorating stress evolutions are believed as the main culprits for battery failure. Based on these new insights, we propose a lithium–tin (Li–Sn) composite anode model with $LiSn_x$ stable skeleton and homogeneous nucleation sites for uniform Li stripping/deposition processes. The ameliorated Li–Sn/electrolyte interface is demonstrated by the significantly reduced stress fluctuations as revealed by FBG sensing. The homogeneous mechanical forces at the Li—Sn/electrolyte interface benefits the cyclic stability of the full cells paired with $LiNi_{0.6}Co_{0.2}Mn_{0.2}O_2$ (NCM) under low uniaxial stack pressures (<2 MPa). This work provides quantitative information for the design of interfacial stress regulation strategies in all-solid-state batteries.

2. Results and Discussion

2.1. Failure of Li Metal Anodes in ASSLBs Under Low Stack Pressure

High uniaxial stack pressures are widely applied for lab-scale pellet-type ASSLBs for enhanced adhesive contact and electrochemical performance. However, they are impractical for real battery packs due to cost, safety and complex Li deposition issues.[23] In this work, we measured the ASSLBs with Li metal anodes (thickness = 100 μm) under a low pressure of 3 MPa (Figure S1, Supporting Information). **Figure 1a** shows the stripping and plating behaviors of a typical Li||PLL||Li solid-state cell at a current density of 0.1 mA cm^{-2} and a capacity of 0.1 mAh cm^{-2}. The symmetric cell presented a soft internal short circuit after 82 h and completely failed after 106 h. The lifespan is much shorter than these in literature with the same cell configurations, which can be ascribed to our low uniaxial stack pressure.[24–27] The short-circuit failure of Li||PLL||Li cell can be verified by the ex-situ EIS measurements, which display interfacial resistances (R_{surf}) of 450, 520, and 0 Ω after the 1st, 20th and 53rd cycles, respectively (Figure 1b). SEM image (Figure 1c) also demonstrates the growth of Li dendrite after plating of 1 mAh cm^{-2}, which potentially penetrates the PLL solid-state electrolyte.

The evolution of interface contacts upon cycling was then investigated without dissembling the Li/PLL assembly. Before cycling, SEM image and the corresponding energy dispersive X-ray (EDX) image present a seamless contact between PLL electrolyte and Li electrode under 3 MPa (Figure 1d,e). After 20 cycles at 0.1 mA cm^{-2} and 0.1 mAh cm^{-2}, significant micro-voids appear at the Li/PLL interface (Figure 1f,g), which intuitively explains the increased interfacial resistance for the Li||PLL||Li cell in Figure 1b. Note that the Li/PLL interface were distinguished by the O signal in Li metal (Li element is invisible under SEM) and the La signal in PLL electrolyte. Overall, the failure of Li metal electrodes in ASSLBs under low stack pressure can be illustrated in Figure 1h. The flexible and flat PLL electrolyte initially establishes favorable interfacial contact with Li metal at moderate stack pressures (Figure S2, Supporting Information). However, due to the heterogeneous nucleation and growth of Li metal, voids and Li dendrites forms at the Li/electrolyte interface. The uneven interface leads to uneven stress and electric field distribution during the Li plating and stripping

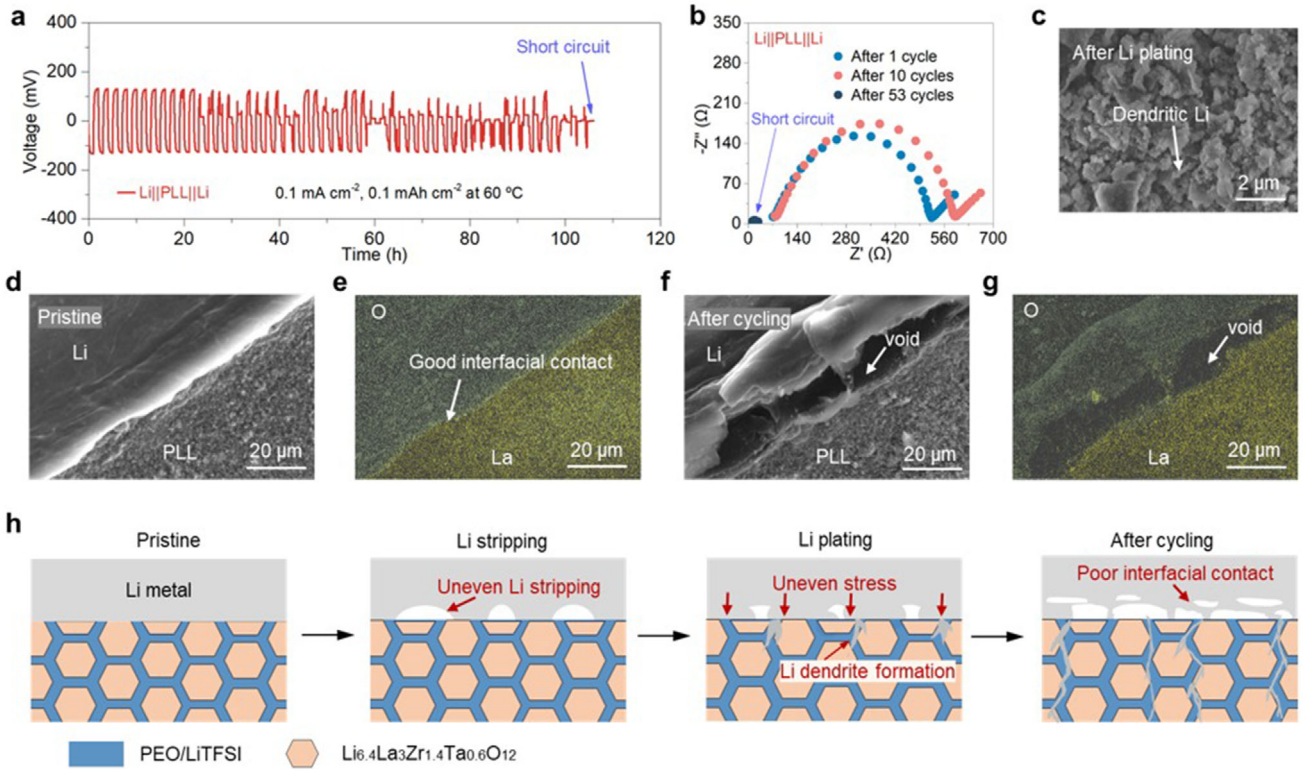

Figure 1. Failure of Li metal anodes in ASSLBs under low stack pressure. a) Voltage profiles for the symmetric Li||PLL||Li cell at 0.1 mA cm^{-2} and 0.1 mAh cm^{-2} at 60 °C. b) Representative EIS spectra for the symmetric Li||PLL||Li cell after 1st, 10th and 53rd cycles at 0.1 mA cm^{-2} and 0.1 mAh cm^{-2}. c) The top-view SEM image of the pure Li electrode after electrochemical Li plating at 0.1 mA cm^{-2} for 10 h. The cross-sectional SEM images and EDS elemental mapping image for O and La of (d,e) the pristine Li/PLL interface and (f,g) after 20 cycles at 0.1 mA cm^{-2} and 0.1 mAh cm^{-2}. h) Schematic illustration for the evolution of Li electrodes upon cycling in ASSLBs under low uniaxial stack pressure. The uneven Li stripping behavior can cause voids formation at the electrode/electrolyte interface, which result in dendritic Li growth and uneven stress distribution. After several cycles, the uneven Li stripping/plating behavior will deteriorate interface contact, and the filamentous Li dendrite has the risk of penetration into solid-state electrolytes.

processes, fostering whisker Li dendrites. The mechanically strong Li whiskers are ready to penetrate into PLL electrolyte and cause short circuit finally. It was reported that the strain of individual Li whiskers scales linearly with the generated stress within the elastic regime, so that continuous Li plating can perpetuate an increase in stress.[10] Given the constant testing conditions (uniaxial stack pressure and temperature) and the solely lithium plating and stripping as the prevailing electrochemical process, it is reasonable to ascribe the lithium deposition and stripping as the primary cause of the stress. Therefore, operando measurement and quantification of stress are pivotal in disentangling the relationship between Li plating-induced stress and mechanical failure in ASSLBs.

2.2. Operando Monitoring of Strain Amplitude and Heterogeneity at Li/Electrolyte Interface

FBG sensor was implanted into the Li||PLL||Li cells to operando monitor the stress evolution at the electrode/electrolyte interface during cycling under low stack pressures.[22] **Figure 2a** describes the working principle of FBG sensor. When light travels through the Bragg grating of FBG optical fiber, only a specific wavelength, named as Bragg wavelength (λ_B), will be reflected. The Bragg wavelength is defined by the equation, $\lambda_B = 2n_{eff}\Lambda$, where n_{eff} represents the effective refractive index of the grating and Λ is the Bragg grating period. Any variations in temperature (T) and strain (ε) surrounding the FBG sensor will induce changes of the reflected wavelength, manifesting a peak shift, $\Delta\lambda_B$. It is noted that the miniature silica FBG sensors (Φ = 125 μm) inserted in Li||PLL||Li Swagelok cells (Figure 2b,c) can suppress the adverse impacts on electrochemical behaviors and possible chemical reactions in various electrochemical environments (Figure S3, Supporting Information).

To quantify the sensitivities of the FBG sensor in this setup, we measured the $\Delta\lambda_B$ at different environmental temperatures and stack pressures (which induce stress field on the sensor) of the Swagelok cells without cycling. Figure 2d,e shows high linearity of the responses, yielding the temperature and stacking pressure sensitivities of 9.3 pm °C^{-1} and 69 pm MPa^{-1}, respectively. Evidently, the FBG sensor presents great sensitivity to the surrounding stress field. To decouple the T-induced optical signal responses from stress changes surrounding the fiber, we designed a temperature-sensitive-only FBG sensor by encasing the FBG fiber within a rigid glass tube to exclude the effect of strain during cycling (Figure 2f). When the Li||PLL||Li Swagelok cell was embedded with the T-sensitive-only FBG fiber and cycled at 0.2 mA cm^{-2} and 0.4 mAh cm^{-2}, the real-time

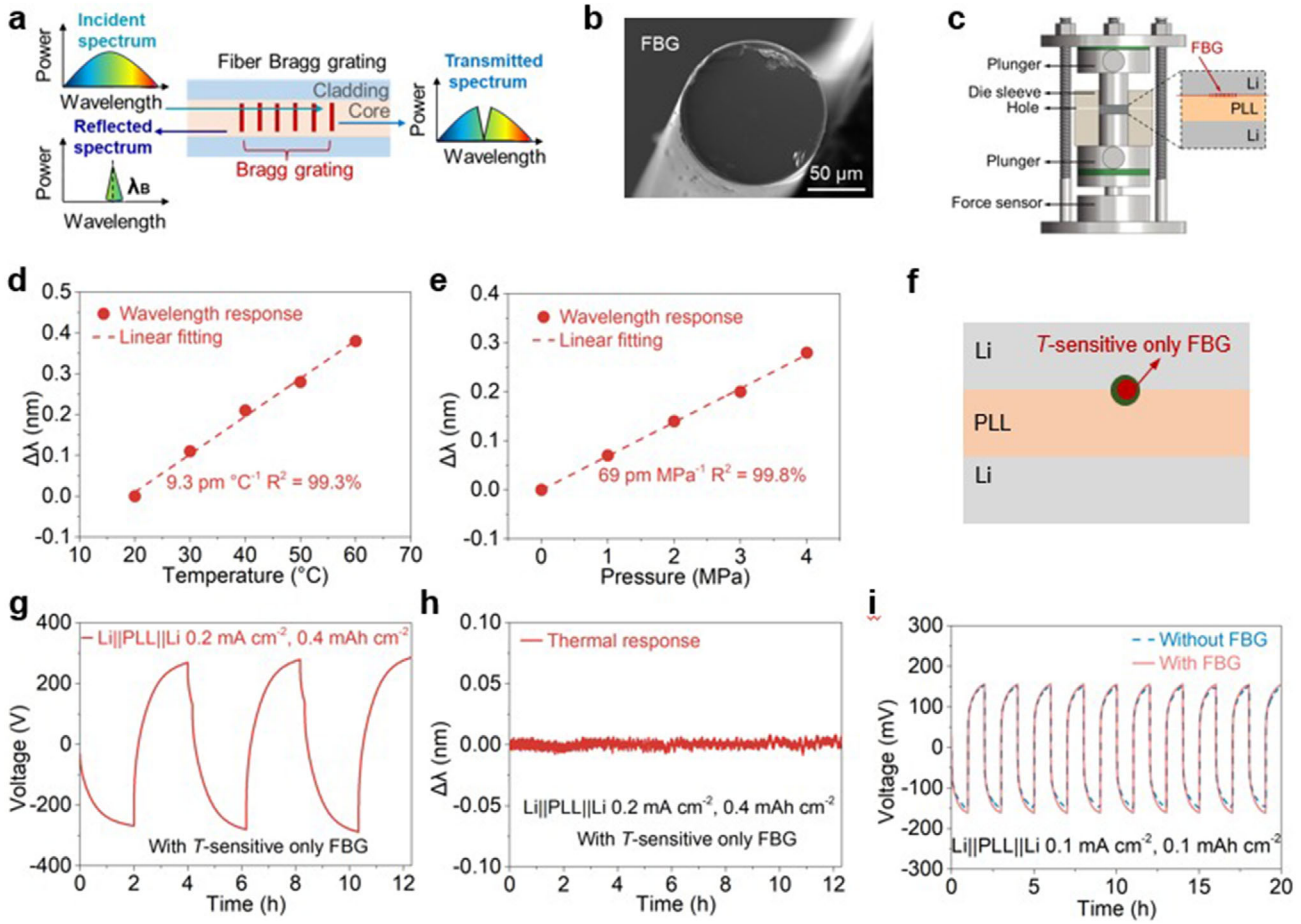

Figure 2. Setup to operando monitor the strain evolutions within ASSLBs. a) Scheme of the working principle of FBG sensors. b) The cross-sectional SEM image of FBG sensor. c) Schematic diagram of the modified Swagelok cell with the implemented FBG sensor and the external force sensor. The wavelength response of FBG sensor upon d) temperature and e) pressure. f) Scheme of the implemented *T*-sensitive-only FBG sensor in the Li||PLL||Li Swagelok cell. g) Cycling performance for the symmetric Li||PLL||Li Swagelok cell at 0.2 mA cm^{-2} and 0.4 mAh cm^{-2} with *T*-sensitive-only FBG sensor. h) The thermal response of *T*-sensitive-only FBG sensor. Note that the cell was cycled in a 60 °C oven. i) Cycling performance for the symmetric Li||PLL||Li Swagelok cells with and without FBG sensor.

thermal response remained nearly constant, indicating that the heat generated from cell cycling put a negligible impact on $\Delta\lambda_B$ (Figure 2g,h). Moreover, by comparing the voltage-time curves of the Li||PLL||Li Swagelok cells with and without the implemented FBG sensors, we corroborate that our FBG sensor does not affect the cell's electrochemical performance (Figure 2i and Figure S4, Supporting Information). The transparency of FBG sensor to the electrochemical behaviors under high-rate and high-capacity conditions is verified in Figure S4 (Supporting Information).

To accurately monitor the strain evolution during Li stripping and plating processes, FBG sensors were embedded at electrode/PLL interface in the Li||PLL||Li Swagelok cells cycling at 0.2 mA cm^{-2} and 0.4 mAh cm^{-2} under a constant uniaxial stack pressure of about 2.4 MPa (measured by external force sensor; **Figure** 3a, top). Regarding the origins of stress, the trivial temperature variation in Figure 2h excludes the contribution of the thermal stress to the following strain signals. Together with the constant uniaxial stack pressure of about 2.4 MPa, the stress variation below could be mainly ascribed to the electrochemical processes, namely, the plating and stripping of lithium. Figure 3b shows temporal evolutions of the reflected spectra of the embedded FBG sensor during the initial three cycles, revealing not only the continuous shifts of Bragg wavelength but also the splitting/broadening of the Bragg peak. Figure S5 (Supporting Information) demonstrates that temperature variations do not affect the broadening of the FBG spectrum. Since FBGs are primarily sensitive to temperature and stress, the broadening of FBG spectra is predominantly arising from changes in stress. This work is the first to reveal the continuous shifts of Bragg wavelength and peak splitting/broadening during cycles through temporal evolutions of FBG spectra, thus providing new opportunities in operando stress monitoring for safe solid-state batteries. The 3D stack view of the reflected spectra (Figure 3c–e) corroborates that gradual splitting of two initial optical resonance peaks (λ_B = 1542.18 and 1542.37 nm) into five peaks (λ_B = 1542.23, 1542.58, 1542.91, 1543.54, and 1543.55 nm) after three cycles. The evolution from birefringence (due to the pre-applied pressure of

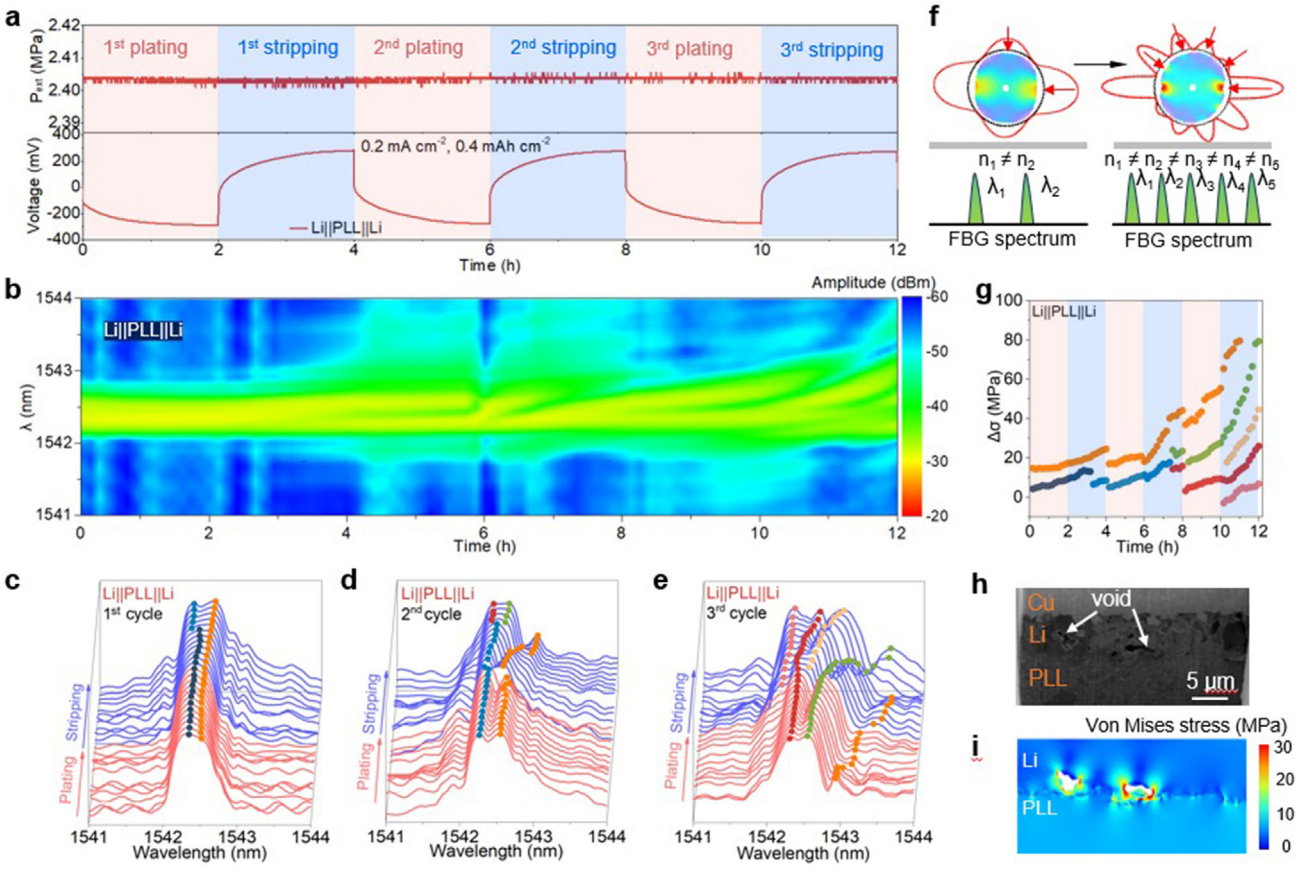

Figure 3. Operando monitoring of strain amplitude and heterogeneity at Li/electrolyte interface. a) Cycling performance for the symmetric Li||PLL||Li Swagelok cells at 0.2 mA cm^{-2} and 0.4 mAh cm^{-2} together with the stack pressure. b) Real-time spectral responses of the implemented FBG sensor in the symmetric Li||PLL||Li Swagelok cells during cycling shown in (a). c–e) 3D stack-view of the real-time spectral responses for the FBG sensor located at the Li/PLL interface in the symmetric Li||PLL||Li Swagelok cell. f) Scheme of the transition from birefringence to multi-refringence phenomena for the implemented FBG sensor in the symmetric Li||PLL||Li Swagelok cell upon cycling. g) $\Delta\sigma$-time plot from the FBG sensor in the symmetric Li||PLL||Li Swagelok cells during the first three cycles. h) FIB-SEM image of the Li/PLL assembly after 3 cycles at 0.2 mA cm^{-2} and 0.4 mAh cm^{-2}. i) COMSOL Multiphysics simulated stress distributions at the Li||PLL interface.

ca. 2.4 MPa) to multi-refringence peaks can be ascribed to the changes for effective refractive index of the waveguide in multi-directions, corresponding to the heterogeneity of the stress field as seen in composite materials.[28,29] Therefore, the increasing peak number stems from the exacerbated anisotropic strain distributions in different regions of the FBG sensor, resulting from inhomogeneous lithium plating, as schematically illustrated in-Figure 1h,f and Figure S6 (Supporting Information).[19,29,30] In addition, the broadening of the spectra with cycling also suggests the presence of divergent strain states and thereby non-uniform strain distribution surrounding the FBG sensor. It is noteworthy that the FBG sensor in the Li||PLL||Li Swagelok cell exhibits a flat baseline with a single optical resonance peak before pressurization (Figure S7, Supporting Information). The birefringence arising from a low uniaxial stack pressure of 2.4 MPa (Figure 3c and Figure S8, Supporting Information) validates the capability of FBG sensors to capture the heterogeneity of stress field within the cell, which is rarely visited in previous few studies.

In an effort to quantify the amplitude of stress (σ) evolution surrounding FBG sensors, we estimated the strain (ε) values from the wavelength shift ($\Delta\lambda_B$, $\Delta\lambda_B = \lambda_B - \lambda_{B,0}$) according to the following equations:[22,31]

$$\frac{\Delta\lambda_B}{\lambda_{B,0}} = \left(1 - \frac{n_{eff}^2\left[P_{12} - \nu\left(P_{11} + P_{12}\right)\right]}{2}\right)\varepsilon \quad (1)$$

$$\sigma = \varepsilon E \quad (2)$$

where $\lambda_{B,0}$ is the initial Bragg wavelength, P_{11} and P_{12} is the strain-optical coefficients of the FBG sensor, ν is the Poisson's ratio, E is the Young's modulus of the FBG sensor. The values of n_{eff}, ν, P_{11}, P_{12}, E of the used FBG sensor is 1.45, 0.17, 0.113, 0.252 and 69.9 GPa, respectively.[18,22] Note that we do not rely on the derived parameters in Figure 2e to infer the stress, because the external pressure in Figure 2e is not consistent with the internal stress in ASSLBs. Moreover, Equations (1) and (2) adopt a few assumptions and we can only provide an estimation of the stress evolutions.[32]

The evolution of stress amplitude at the Li/PLL interface presents a drastic fluctuation with a peak value of 80 MPa at the end of the third cycle (Figure 3g). Additionally, five major stress components (Figure 3g) are identified according to the prominent peaks in the reflected spectra (Figure 3c–e and Figure S9, Supporting Information), implying the heterogeneous stress from at least five different directions at the interface. Intuitively, the buildup of internal stress and heterogeneous stress field very likely mirror and quantify the extent of anisotropic stripping/plating of lithium (Figure 1c). To validate the above link, we further bridge the stress field and anisotropic lithium stripping/plating via the finite-element analysis (COMSOL Multiphysics simulation).[33] The geometry of the Li/PLL interface after 3-cycle lithium plating and stripping was extracted by the focused ion beam (FIB)-SEM image (Figure 3h). It was then input into the model to simulate stress field at the interface after 3 cycles (see the results in Figure 3i). The simulation results show uneven stress distributions at the interface of Li/PLL with stresses ranging from 5 to 30 MPa, which is in the same order of the measured stresses (Figure 3g). The combined effects of pore geometry and interfacial modulus mismatch drive stress accumulation at the interface center, exceeding edge stresses and increasing susceptibility to delamination or microcrack initiation (Figure S10, Supporting Information). The unfavorable electrode structure evolution behavior is one of the main driving forces behind the uneven distribution of stress. The uneven stress distribution is detrimental and likely accelerates the formation/growth of lithium dendrite (as seen in Figure 1f–h), considering the pressure-dependent nature of lithium plating/stripping.[34,35] Thus, the heterogeneity in stress corresponds to the strain of dendritic Li filaments, which is intrinsically related to the porosity of Li metal deposits, and is the main culprit causing battery short circuits and uneven stress distribution.

2.3. Operando Strain Sensing with Dendrite-Free Li–Sn Composite Anodes

The above findings unfold the links between lithium plating/stripping behaviors and the interfacial stress field sensed by the optical fiber sensor. Namely, uneven plating/stripping behaviors of bare Li metal render heterogeneous stress distribution and aggravate the non-uniform electrochemical reactions (**Figure 4**a). To accommodate the chemo-mechanical induced failure and further examine the sensing approach, we propose a Li—Sn composite model architecture with lithiophilic $Li_{22}Sn_5$ alloy as the stable skeleton and the homogeneous nucleation sites for dendrite-free Li deposition (Figure 4b).[36–41] The AFM results demonstrate that the Young's modulus of the Li—Sn composite foil is 5.9 GPa, slightly higher than the 4.9 GPa of the pure Li (Figure S11, Supporting Information). Considering the extremely high molar ratio of lithium atoms (172:2 for Li to Sn), the Li—Sn electrode has similar Poisson's ratio to the pure lithium electrode. Noteworthy is that the Li—Sn composite electrode with high specific capacities can be manufactured by a scalable roll-to-roll process for practical applications in ASSLBs (Figure S12, Supporting Information). The similar Li stripping voltage plateau to the pure Li anode also indicates that active Li is provided by over-stoichiometric metallic Li matrix in the Li—Sn composite electrode rather than the $Li_{22}Sn_5$ alloy. The comparable Li stripping voltage plateaus and specific capacity of the Li—Sn composite electrode are beneficial for high-energy solid-state Li metal batteries (Figure S12, Supporting Information). Similarly, we constructed Li—Sn||PLL||Li—Sn Swagelok cells and measured the stress distribution via FBG sensors during cycling at a current density of 0.2 mA cm^{-2} and a capacity of 0.4 mAh cm^{-2} (Figure 4c) with an external stack pressure of ca. 2.4 (Figure 4c, top). The time-resolved voltage curve shows stably cycling behaviors for Li—Sn electrodes with a smaller overpotential of 163 mV than the 286 mV of Li||PLL||Li cells, due possibly to the enhanced structural integrity and more uniform stress field.

Unlike Li||PLL||Li, the temporal reflected spectra of embedded FBG at Li—Sn/PLL interface (Figure 4d) show little changes of λ_B with two stable peaks at 1588.35 and 1588.64 nm throughout the entire testing period. The absence of visible peak broadening/splitting indicates a relatively stable and uniform stress field at the interface. The 3D stack-view of the spectra confirm the well-reserved birefringence and thereby stress field in the cycling (Figure 4e–h). Different from the severe fluctuations of stress at the Li/PLL interface, the stresses at Li—Sn/PLL interface only slightly shift upon cycling (Figure 4i and Figure S13, Supporting Information). The absence of reversible strain changes during lithium plating and stripping processes may result from the negligible net volume changes in symmetrical Li—Sn||PLL||Li—Sn configuration and the low modulus (≈380 MPa) of the hybrid solid-state electrolyte in this work.[22,42] Moreover, the maximum stress of Li—Sn/PLL interface (≈12 MPa) is substantially lower than that of Li/PLL (≈80 MPa), indicating the suppressed stress concentration at the interface. It is worth noting that the $Li_{22}Sn_5$ alloy framework uniformly distributed in the composite electrode is stable during the lithium plating/stripping process, which is conducive to buffer volume changes (Figure S14, Supporting Information). The simulation result also verifies a much more stable interface with a highly uniform stress field (Figure 4j, see the SEM image in Figure S15, Supporting Information). Shortly, the homogeneous nucleation on the surface of Li—Sn electrode inhibits the growth of anisotropic dendritic Li and thus maintains the uniform stress field at the interface, which, in turn, suppresses the uneven plating/stripping of lithium (Figure 4b). The above results together with data of longer cycles (Figure S16, Supporting Information) indicate that the uneven distribution of stress may the primary contributor to the chemomechanical failure of the solid-state cells. These encouraging results again highlight the importance of monitoring chemo-mechanics at the interface of ASSLBs.

2.4. Electrochemical Performance of Li—Sn Composite Anode in ASSLBs

To confirm the positive role of uniform stress distribution on stabilizing the Li—Sn composite anodes, we conducted Li plating and stripping tests for Li—Sn||PLL||Li—Sn and Li||PLL||Li cells at 60 °C. The thicknesses of Li—Sn composite and Li metal electrodes are identical (Figure S17, Supporting Information). **Figure 5**a shows the cyclic performance of Li—Sn||PLL||Li—Sn cell with an impressive stability of over 3000 h at 0.1 mA cm^{-2}

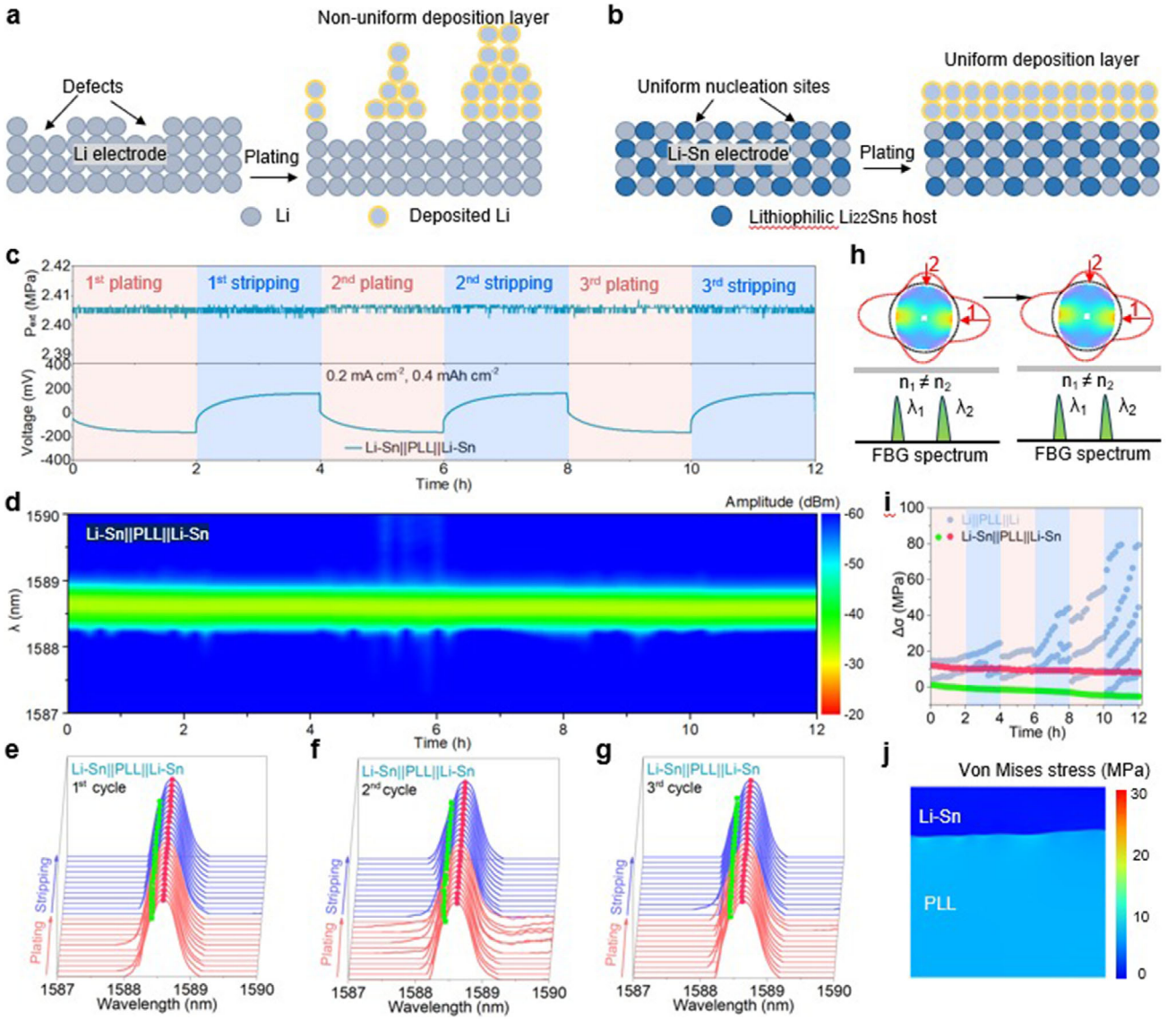

Figure 4. Operando strain sensing with dendrite-free Li—Sn composite anodes. Scheme of the Li plating behaviors on the surface of a) Li and b) Li—Sn electrodes. c) Cycling performance for the symmetric Li—Sn||PLL||Li—Sn Swagelok cells at 0.2 mA cm^{-2} and 0.4 mAh cm^{-2} together with the stack pressure. d) Real-time spectral responses of the implemented FBG sensor in the symmetric Li—Sn||PLL||Li—Sn Swagelok cells as cycling in (c). e–g) 3D stack-view of the real-time spectral responses in d) for the FBG sensor located at the Li—Sn/electrolyte interface in the symmetric Li—Sn||PLL||Li—Sn Swagelok cells. h) Scheme of the remained birefringence phenomena for the implemented FBG sensor in the symmetric Li—Sn||PLL||Li—Sn Swagelok cells upon cycling. i) $\Delta\sigma$-time plots comparison from the FBG sensor in the symmetric Li||PLL||Li and Li—Sn||PLL||Li—Sn Swagelok cells during the first three cycles. j) COMSOL Multiphysics simulation of the stress distribution at the Li—Sn||PLL interface in symmetric cell.

and 0.1 mAh cm^{-2} (corresponding to an accumulative capacity of 300 mAh cm^{-2}), which is much longer than Li||PLL||Li cells. Representative voltage profiles at the 1st, 21st and 1500th cycles present overpotentials of below 40 mV for Li—Sn||PLL||Li—Sn, which are significantly lower than the 150 mV for Li||PLL||Li cells. To further demonstrate the superiority of Li—Sn/PLL assembly over Li/PPL at higher cycling capacities, which could exacerbate the interfacial deterioration, we cycled the Li—Sn||PLL||Li—Sn and Li||PLL||Li cells at 0.25 mA cm^{-2} and 0.5 mAh cm^{-2} (Figure 5b). The former delivered stable potential profiles for 200 h with an overpotential of 70 mV, while the latter experienced a soft short circuit after only 6 cycles and failed after 20 cycles.

The surface of the Li—Sn electrode is covered by homogeneously distributed particles with a diameter of 100 nm after electrochemical stripping at 0.1 mA cm^{-2} for 10 h. These nanoparticles are $Li_{22}Sn_5$ alloy, which are conducive to maintaining stable interfacial contact by providing uniform Li nucleation sites and fast Li-ion diffusion networks (Figure S18 and S19, Supporting Information). The stable interface between Li—Sn composite electrode and PLL electrolyte can be responsible for the long-term cycling for Li—Sn||PLL||Li—Sn cells. As depicted in

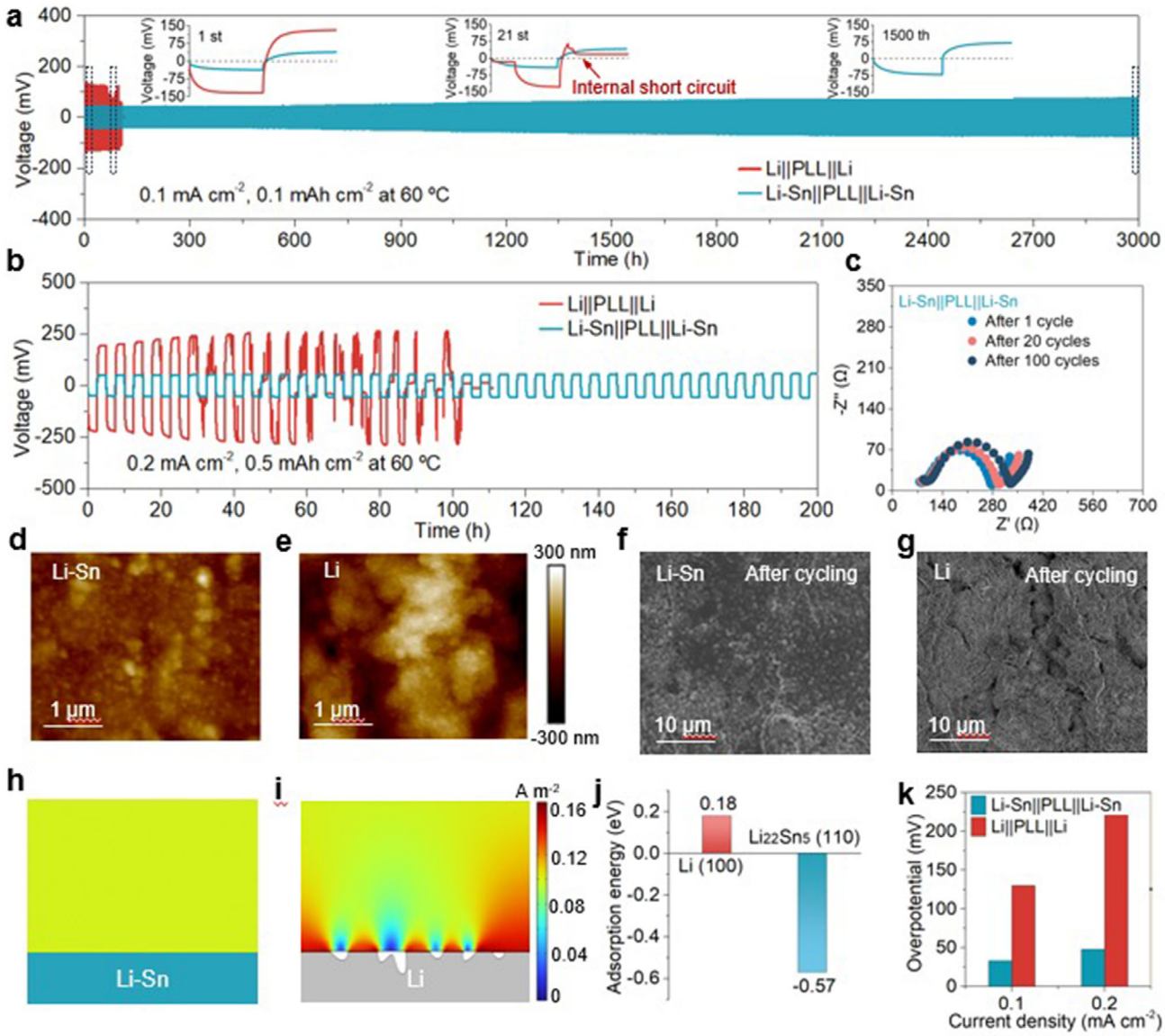

Figure 5. Electrochemical performance of Li—Sn and Li in symmetric cells. a) Long-term cycling and the enlarged profiles at selected cycles for the symmetric Li—Sn||PLL||Li—Sn and Li||PLL||Li coin-type cells at 0.1 mA cm^{-2} and 0.1 mAh cm^{-2} at 60 °C. b) Cycling for the symmetric Li—Sn||PLL||Li—Sn and Li||PLL||Li cells at 0.2 mA cm^{-2} and 0.5 mAh cm^{-2} at 60 °C. c) Representative EIS spectra for the symmetric Li—Sn||PLL||Li—Sn cells after selected cycles at 0.1 mA cm^{-2} and 0.1 mAh cm^{-2}. AFM images of surface of d) the Li—Sn electrode and e) Li electrode. Top-view SEM images of f) the Li—Sn and g) Li electrodes after 20 cycles at 0.1 mA cm^{-2} and 0.1 mAh cm^{-2}. COMSOL Multiphysics simulations of the current distribution at the h) Li—Sn||PLL and i) Li||PLL interface. j) Li adsorption energies on Li (100) and $Li_{22}Sn_5$ (110). k) Overpotential for Li nucleation on Li and Li—Sn electrodes at different current densities.

Figure 5c, the interface resistance of Li—Sn||PLL||Li—Sn cell almost maintains intact at 200 Ω from the 1st cycle to the 20th cycle, and slightly increased to 240 Ω after 100 cycles. These interface resistances are smaller and more stable than these for Li||PLL||Li cell (Figure 1b), which exhibits a short circuit behavior after 51 cycles. The morphologies of cycled Li metal and Li—Sn electrodes can provide direct information for evaluating the interfacial stabilities. Top-view AFM and SEM images of the Li—Sn composite and Li electrodes show smooth surface in their pristine states (Figure 5d,e and Figure S20, Supporting Information). A flat surface is also demonstrated for the PLL electrolyte, which eliminates the possible instability caused by large surface roughness of the electrolyte (Figure S21, Supporting Information). After plating/stripping Li metal at 0.1 mA cm^{-2} and 0.1 mAh cm^{-2} for 20 cycles, a smooth and dense surface morphology is preserved for the Li—Sn electrode (Figure 5f). In sharp contrast, the pure Li electrode exhibits a rough surface covered with micrometer-scale cracks and ubiquitous dendritic Li, which are culprits for subsequent internal short circuits (Figure 5g).

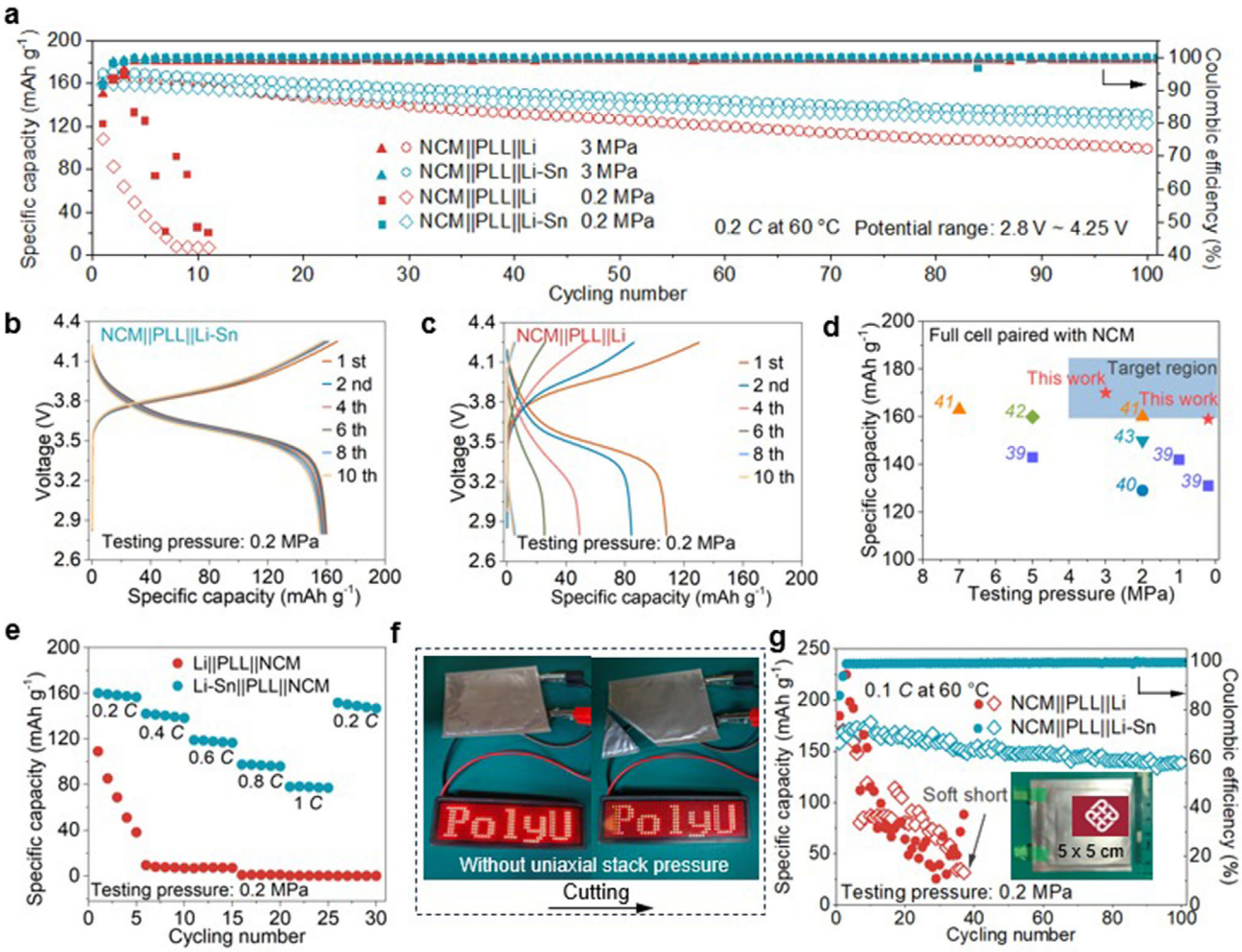

Figure 6. Electrochemical performance of ASSLB full cells. a) Cycling performance of the NCM||PLL||Li—Sn and NCM||PLL||Li full cells at 0.2 *C* under different uniaxial stack pressures. b,c) The voltage profiles of b) the NCM||PLL||Li—Sn and c) the NCM||PLL||Li full cells for selected cycles under low stack pressure of 0.2 MPa in (a). d) Comparison of specific capacities and testing pressures for ASSLBs using NCM cathode in this work with previously reports. e) Rate performance of the NCM||PLL||Li—Sn and NCM||PLL||Li full cells under a low stack pressure of 0.2 MPa. f) Non-pressed NCM||PLL||Li—Sn pouch cell lighting a LED bulb before and after cutting. g) Cycling performance of the NCM||PLL||Li—Sn and NCM||PLL||Li pouch cells at 0.1 C. The inset is a photo image of the pouch cell.

The chemo-mechanical behavior and the interfacial evolution were further investigated by theoretical simulations. Finite-element calculations were conducted to reveal the current distribution at the Li—Sn/PLL and Li/PLL interfaces (Figure 5h,i). Consistent to the SEM images in Figure 5f,g, the Li—Sn/PLL interface exhibits a uniform current distribution with the conformal contact, whereas the Li/PLL interface shows a highly uneven current distribution across the interface, with lower current at voids and higher current at contact regions. The non-uniform current distribution is a primary cause of dendritic Li growing, leading to the non-uniform stress distribution and the degraded interfacial contact. Density functional theory (DFT) calculations determined the Li adsorption energies on $Li_{22}Sn_5$ (110) and Li (100) surface to be −0.57 and 0.18 eV, respectively (Figure 5j).[43,44] The lower Li adsorption energy on Li—Sn alloy is beneficial for facilitating the uniform deposition and homogeneous nucleation of Li metal, thereby inhibiting the formation of dendritic Li. The theoretical speculation is corroborated by the reduced Li nucleation overpotential for Li—Sn composite electrode compared to Li electrode at 0.1 and 0.2 mA cm^{-2} (Figure 5k). These findings indicate that integrating Li—Sn composite anode can effectively mitigate anode/electrolyte interfacial deterioration by maintaining the interface contact, regulating Li stripping/plating processes, and suppressing Li dendrites growth and the interface stress fluctuations.

To demonstrate the practical feasibility of Li—Sn anodes in ASSLB applications, we fabricated full cells using micro-sized NCM particles (10-20 µm) as the cathode material (Figure S22, Supporting Information). The PLL electrolyte exhibited a high anodic stability up to 4.8 V for the high-voltage NCM cathodes (Figure S23, Supporting Information). **Figure 6**a shows the cycling performance of the NCM||PLL||Li—Sn and NCM||PLL||Li cells at a current density of 0.2 C (1 C = 170 mA g^{-1}) in the voltage range of 2.8–4.25 V at 60 °C under a low uniaxial stack pressure of 3 MPa. Impressively, the NCM||PLL||Li—Sn cell delivers

a high discharge capacity of 132 mAh g^{-1} after 100 cycles, corresponding to 77.6% of the initial capacity (170 mAh g^{-1}). The capacity degradation is mainly attributed to the inevitable volumetric changes of NCM particles under low stack pressure, which can cause partial contact failure between the NCM and solid-state electrolyte.[45] In contrast, the NCM||PLL||Li cell displayed a dramatic capacity degradation from 167 mAh g^{-1} to 99 mAh g^{-1}, with a much lower capacity retention of 59.3% over 100 cycles.

Under an even lower uniaxial stack pressure of 0.2 MPa, the NCM||PLL||Li—Sn cell demonstrates a high specific capacity of 159 mAh g^{-1} and considerable capacity retention of 77.4% over 100 cycles. Conversely, the NCM||PLL||Li full cells delivered a significantly lower specific capacity of 108 mAh g^{-1} and fast capacity decay due to the deteriorated interface stability. The NCM||PLL||Li—Sn full cell demonstrates stable voltage profiles upon cycling, whereas the NCM||PLL||Li cell showed larger potential hysteresis and short voltage plateaus (Figure 6b,c). The specific capacities for NCM||PLL||Li—Sn cells surpass many recently reported values and satisfies the target benchmarks (Figure 6d).[45–49] Additionally, the rate capability under 0.2 MPa for the NCM||PLL||Li—Sn cell also outperforms that for the NCM||PLL||Li cell (Figure 6e), retaining higher specific capacities at high rates (112 mAh g^{-1} at 0.8 C and 95 mAh g^{-1} at 1 *C*) than the NCM||PLL||Li counterpart, which only offers 110 mAh g^{-1} at 0.2 C and rapidly decays in subsequent cycles (Figure S24, Supporting Information). The improved rate performance can be attributed to the enhanced reaction kinetics from the Li—Sn composite electrode and the well-maintained interface.

To further verify the practical potential of the Li—Sn anodes, NCM||PLL||Li—Sn pouch cells were assembled. When connected to a red light-emitting diode (LED), the NCM||PLL||Li—Sn pouch cell successfully lit the LED before and after cutting, demonstrating impressive safety and workability without uniaxial stack pressure (Figure 6f). The cycling performance of the NCM||PLL||Li—Sn pouch cells showed high-capacity retention of 87.9% for 100 cycles at 0.1 *C* with stable charge/discharge processes, compared to the NCM||PLL||Li cells (Figure 6g), which exhibited violent voltage fluctuations and a subsequent short circuit after 35 cycles. Moreover, the full cells with Li—Sn anodes deliver higher Coulombic efficiencies (CEs) than these using Li metal anodes (Figure 6a,g). Specifically, the initial CEs for NCM||Li—Sn are 92.5% at 3 MPa and 91.1% at 0.2 MPa in coin cells and 85.8% at 0.2 MPa in pouch cells, which are much higher than the 88.8%, 79.8% and 74.4% for the NCM||Li counterparts. Considering the large-scale fabrication feasibility of the PLL electrolyte and the Li—Sn composite electrode (Figure S25, Supporting Information), the Li—Sn/PLL integration in this work presents significant potential for commercializing high-energy ASSLBs.

3. Conclusion

We utilized FBG sensor to operando monitor stress variation at anode/electrolyte interface during Li stripping/deposition process to reveal the chemo-mechanical failure mechanisms of ASSLBs under low stack pressures. By tracking reflected spectra of FBG with Li stripping and plating, the evolving amplitude and heterogeneity of stress at the anode/electrolyte interface was quantitatively analyzed. For the first time, the broadening and splitting of Bragg peaks were carefully monitored to assess the heterogeneity of stress in ASSLBs, which is essential but difficult for operando stress tracking previously. The as-developed approach revealed severe stress concentration and buildup at Li/electrolyte interface, due to the uncontrolled growth of dendritic Li. Combined with electrochemical testing and simulations, we further disclose the interplay between uneven Li stripping/plating and the non-uniform stress field in ASSLBs. To suppress the uneven Li stripping/plating, we proposed a Li—Sn composite electrode with uniform nucleation sites, rendering a stable interface and a homogeneous stress field as sensed by the FBG. The Li—Sn electrode therefore delivers excellent performance in both symmetric and full cells under low stack pressure. This work not only elaborates the FBG spectra for operando monitoring the amplitude and heterogeneity of interfacial stress in ASSLBs, but also highlights the critical role of homogenizing stress distribution in maintaining interface contact, and offers chemo-mechanical insights into the rational design of anode electrode toward reliable low-pressure ASSLBs.

4. Experimental Section

Preparation of the Li—Sn Composite Foil and Hybrid Solid-State Electrolyte: Li—Sn composite foil was fabricated via repeated mechanical kneading operations of Li foil (China Energy Lithium) and Sn foil (Sigma Aldrich) at room temperature. The mass ratio of Li foil to Sn foil was chosen as 5:1. During the repeated calendaring and folding operations, the wrapped Sn foil gradually reacted with metallic Li to form $Li_{22}Sn_5$ alloy ($Li + 5Sn \rightarrow Li_{22}Sn_5$), which is a thermodynamic favorable process. All fabrication processes were carried out in a glove box under argon atmosphere (< 1 ppm H_2O and O_2). To prepare hybrid solid-state electrolyte, polyethylene oxide (PEO, MW = 600 000, Sigma Aldrich) and lithium bis(trifluoromethanesulfonyl)imide LiTFSI (Sigma Aldrich) were mixed with acetonitrile and intensively stirred for 24 h at 60 °C, wherein the molar ratio of PEO to Li was 18:1. Then, $Li_{6.4}La_3Zr_{1.4}Ta_{0.6}O_{12}$ (LLZTO) nanoparticles (Sigma Aldrich) were added into the as-obtained transparent solution and intensively stirred for 2 h, wherein the mass ratio of LLZTO to PEO/LiTFSI was 1:1. The obtained homogeneous viscous slurry was then cast onto the fixed silicone release paper with a doctor blade and dried in vacuum for 72 h at 60 °C and baked in glove box under argon atmosphere for 72 h at 50 °C to thoroughly remove residual acetonitrile. The as-prepared hybrid solid-state electrolyte thereinafter is referred to as PLL.

Materials Characterization: X-ray diffraction (XRD) patterns were recorded on a Rigaku SmartLab X-ray diffractometer with Cu Kα radiation (λ = 1.54 Å). Note that the air sensitive samples (e.g., Li and Li—Sn) were sealed with Kapton tape to isolate from oxygen and moisture in a glove box under argon atmosphere before testing. Scanning electron microscopy (SEM) and the corresponding energy dispersive X-ray spectroscopy (EDS) mapping of samples were conducted on a Tescan MAIA3 field emission scanning electron microscopy. Surface morphology images of the samples were acquired with a Bruker Dimension Icon atomic force microscope (AFM). Focused ion beam (FIB)-SEM measurements were carried out using a Helios 5 UX dual-beam focused ion beam system.

Assembly of All Solid-State Swagelok Cells Embedded with FBG Sensors: The Swagelok cell (diameter = 14 mm) was drilled with two through-holes (diameter = 0.8 mm) for the FBG sensor (diameter = 0.125 mm) to pass through. First, the Li—Sn or the pure Li electrode (diameter = 12 mm) was positioned on the center of the bottom plunger of the Swagelok mold. Next, the FBG sensor was passed through the holes and adjusted to ensure the FBG grating (length = 10 mm) locating at the center of the electrode and was fixed with cured epoxy. Then, the PLL electrolyte and the other symmetric electrode was aligned sequentially in the Swagelok's body and were compressed with the top plunger.

The reflected spectra were acquired with the LUNA Si255 interrogator (Micro Optics, USA) with a wavelength accuracy/resolution of 1 pm. The FBG sensors (Grating length = 10 mm) were purchased from SAMYON company (China). The temperature-sensitive (*T*-sensitive) only FBG sensor was fabricated by wrapping the bare FBG with hard glass tube to shield the effect of strain resulted from the changes in thickness of the electrodes during cycling.

Electrochemical Measurements: To evaluate the electrochemical performance, CR-2025 coin-type cells and the pouch cells with double-sided cathodes (5 cm x 5 cm) and two anodes were assembled in an argon-filled glove box using solid-state PLL electrolyte. To prepare NCM electrodes, NCM powders (BASF Shanshan), LLZTO, PEO/LiTFSI and Ketjen black (w:w:w:w = 55:35:5:5) were mixed in acetonitrile and intensively stirred for 24 h at 60 °C. The as-obtained black viscous slurry was then cast onto the aluminum foil and dried in vacuum for 48 h at 60 °C with a subsequent baking in glove box under argon atmosphere for 24 h at 50 °C. The NCM active material loading was about 3.8 mg cm^{-2}. Galvanostatic charge/discharge tests of the coin cells and the pouch cells were conducted on a high-accuracy LAND battery tester (G340A_V5C5AT8). Electrochemical impedance spectroscopy (EIS) measurements and linear sweep voltammetry (LSV) measurements were conducted on a Biologic VMP3 electrochemistry workstation.

Calculations: A computational analysis using COMSOL Multiphysics software was conducted to investigate current density distribution and the stress distributions at the electrode-electrolyte interfaces in symmetric Li||PLL||Li and Li—Sn||PLL||Li—Sn Swagelok cells. For the current distribution simulation, we used the electrochemical module provided by COMSOL MULTIPHYSICS, set the electrode current density of 0.1 mA cm^{-2}, and observed the transient results at 100 us. The grid division of the model is controlled by physical field, and the mesh size is not further modified.

For the stress distribution simulation, to simplify the model and precisely reflect the symmetric structure of the Swagelok cells, a 2D solid mechanics model was employed, focusing on one side of the electrode-electrolyte interface with a width of 40 µm. The construction of 2D geometry model is based on the experimental results shown in SEM and FIB-SEM images. At the bottom surface of the electrolyte region, a fixed boundary condition was imposed. A defined compression pressure was applied at the top surface of the electrode region to simulate the stack pressure applied in the symmetric cell configuration, which was determined from an outer force sensor. The electrode-electrolyte interface was modelled using a contact pair approach based on the augmented Lagrange method. Linear elasticity assumptions were made for the Li, Li—Sn, and PLL materials, and relative parameters are outlined in Table S1 (Supporting Information). Due to the substantial atomic ratio of Li to Sn (171:2), the Young's modulus and Poisson ratio of Li—Sn were set equal to those of Li. The densities of PLL and Li—Sn were derived from the practical synthesis ratio.

First principles calculations were implemented by the Vienna Ab initio Simulation Package[43] The calculated crystal faces are Li (100) and $Li_{22}Sn_5$ (110) surfaces, both of which demonstrated the lowest surface energy among their possible surface orientations.[50] The kinetic energy cutoff was set to be 550 eV. The force convergence criterion was set to be −0.01 eV A^{-1}. All the calculations achieved convergence conditions. The adsorption energy was calculated by subtracting the total energy after adsorption from the energy of each component before adsorption.

Supporting Information

Supporting Information is available from the Wiley Online Library or from the author.

Acknowledgements

J.H. thanks for the financial support of the National Key R&D Program of China (No. 2023YFB2503600). The work described in this work was supported by the Research Centre for Deep Space Exploration (Project No. 1-BBDC), Research Institute for Advanced Manufacturing (Project No, 1-CDK1, 1-CD9C) at the Hong Kong Polytechnic University, and RGC Collaborative Research Fund (Project No. C6047-23G). This work was also supported by research grants from the National Natural Science Foundation of China (No. 52207230 and 92372109), the Guangzhou-HKUST(GZ) Joint Funding Program (No. 2023A03J0003 and No. 2023A03J0103), and the Guangzhou Municipal Science and Technology Project (No. 2024A04J4216). The authors are indebted to the Materials Characterization and Preparation Facility and Laboratory for Brilliant Energy Science and Technology (BEST Lab) of The Hong Kong University of Science and Technology (Guangzhou) for the material characterizations, facility and service supports.

Conflict of Interest

The authors declare no conflict of interest.

Author Contributions

G.L., T.Z. and J.T. contributed equally to this work. Z.L.X. and J.H. conceived the idea and designed the experiments. G.L. and T.Z. carried out the electrochemical and optical measurements with the help of J.T., J.Y. and X.L. for building the experimental setup. M.L. and J.T. performed the simulation and calculations. G.L., Y.X., C.D. and X.H. analyzed the data. Y.K. helped to revise the manuscript. All authors contributed to the preparation of the paper.

Data Availability Statement

The data that support the findings of this study are available in the supplementary material of this article.

Keywords

electrochemical performance, interfacial evolution, lithium–tin alloy, optical fiber sensing, solid state battery

Received: November 16, 2024
Revised: April 28, 2025
Published online: May 15, 2025

[1] Y. S. Meng, V. Srinivasan, K. Xu, *Science* **2022**, *378*, abq3750.
[2] J. Liu, Z. Bao, Y. Cui, E. J. Dufek, J. B. Goodenough, P. Khalifah, Q. Li, B. Y. Liaw, P. Liu, A. Manthiram, Y. S. Meng, V. R. Subramanian, M. F. Toney, V. V. Viswanathan, M. S. Whittingham, J. Xiao, W. Xu, J. Yang, X.-Q. Yang, J.-G. Zhang, *Nat. Energy* **2019**, *4*, 180.
[3] G. Li, X. Duan, X. Liu, R. Zhan, X. Wang, J. Du, Z. Chen, Y. Li, Z. Cai, Y. Shen, Y. Sun, *Adv. Mater.* **2022**, *35*, 2207310.
[4] X. Duan, Y. Li, K. Huang, S. Tu, G. Li, W. Wang, H. Luo, Z. Chen, C. Li, K. Cheng, X.-X. Wang, L. Wang, Y. Sun, *Sci. Bull.* **2025**, *70*, 914.
[5] Q. Zhao, S. Stalin, C.-Z. Zhao, L. A. Archer, *Nat. Rev. Mater.* **2020**, *5*, 229.
[6] X. Hui, Z. Zhan, Z. Zhang, J. Yu, P. Jiang, Z. Dang, J. Wang, S. Cai, Y. Wang, Z.-L. Xu, *ACS Nano* **2024**, *18*, 25237.
[7] Y. Li, E. Mao, Z. Min, Z. Cai, Z. Chen, L. Fu, X. Duan, L. Wang, C. Zhang, Z. Lu, W. Liu, Z. W. Seh, Y. Sun, *ACS Nano* **2023**, *17*, 19459.
[8] X. Peng, Q. Tu, Y. Zhang, K. Jun, F. Shen, T. Ogunfunmi, Y. Sun, M. C. Tucker, G. Ceder, M. C. Scott, *Sci. Adv.* **2024**, *9*, abq3285.
[9] H. Wan, Z. Wang, W. Zhang, X. He, C. Wang, *Nature* **2023**, *623*, 739.
[10] C. Lee, J. Y. Kim, K. Y. Bae, T. Kim, S.-J. Jung, S. Son, H.-W. Lee, *Energy Storage Mater.* **2024**, *66*, 103196.

[11] J. Huang, C. Li, D. Jiang, J. Gao, L. Cheng, G. Li, H. Luo, Z.-L. Xu, D.-M. Shin, Y. Wang, Y. Lu, Y. Kim, *Adv. Funct. Mater.* **2025**, *35*, 2411171.
[12] S. Randau, D. A. Weber, O. Kötz, R. Koerver, P. Braun, A. Weber, E. Ivers-Tiffée, T. Adermann, J. Kulisch, W. G. Zeier, F. H. Richter, *J. Janek, Nat. Energy* **2020**, *5*, 259.
[13] L. Zhang, T. Yang, C. Du, Q. Liu, Y. Tang, J. Zhao, B. Wang, T. Chen, Y. Sun, P. Jia, H. Li, L. Geng, J. Chen, H. Ye, Z. Wang, Y. Li, H. Sun, X. Li, Q. Dai, Y. Tang, Q. Peng, T. Shen, S. Zhang, T. Zhu, J. Huang, *Nat. Nanotechnol.* **2020**, *15*, 94.
[14] Z. Ning, G. Li, D. L. R. Melvin, Y. Chen, J. Bu, D. Spencer-Jolly, J. Liu, B. Hu, X. Gao, J. Perera, C. Gong, S. D. Pu, S. Zhang, B. Liu, G. O. Hartley, A. J. Bodey, R. I. Todd, P. S. Grant, D. E. J. Armstrong, T. J. Marrow, C. W. Monroe, P. G. Bruce, *Nature* **2023**, *618*, 287.
[15] K. S. C. Kuang, R. Kenny, M. P. Whelan, W. J. Cantwell, P. R. Chalker, *Compos. Sci. Technol.* **2001**, *61*, 1379.
[16] X. Han, H. Zhong, K. Li, X. Xue, W. Wu, N. Hu, X. Lu, J. Huang, G. Xiao, Y. Mai, T. Guo, *Light Sci. Appl.* **2024**, *13*, 24.
[17] C. Gervillié-Mouravieff, C. Boussard-Plédel, J. Huang, C. Leau, L. A. Blanquer, M. B. Yahia, M. L. Doublet, S. T. Boles, X. H. Zhang, J. L. Adam, J. M. Tarascon, *Nat. Energy* **2022**, *7*, 1157.
[18] Y. Zhang, X. Xiao, W. Chen, Z. Zhang, W. Li, X. Ge, Y. Li, J. Xiang, Q. Sun, Z. Yan, Y. Yu, H. Yang, Z. Li, Y. Huang, *Small* **2024**, *20*, 2311299.
[19] J. Huang, L. Albero Blanquer, J. Bonefacino, E. R. Logan, D. Alves Dalla Corte, C. Delacourt, B. M. Gallant, S. T. Boles, J. R. Dahn, H.-Y. Tam, J.-M. Tarascon, *Nat. Energy* **2020**, *5*, 674.
[20] Y. Li, Y. Zhang, Z. Li, Z. Yan, X. Xiao, X. Liu, J. Chen, Y. Shen, Q. Sun, Y. Huang, *Adv. Sci.* **2022**, *9*, 2203247.
[21] Z. Miao, Y. Li, X. Xiao, Q. Sun, B. He, X. Chen, Y. Liao, Y. Zhang, L. Yuan, Z. Yan, Z. Li, Y. Huang, *Energy Environ. Sci.* **2022**, *15*, 2029.
[22] L. Albero Blanquer, F. Marchini, J. R. Seitz, N. Daher, F. Bétermier, J. Huang, C. Gervillié, J.-M. Tarascon, *Nat. Commun.* **2022**, *13*, 1153.
[23] C. Fang, B. Lu, G. Pawar, M. Zhang, D. Cheng, S. Chen, M. Ceja, J.-M. Doux, H. Musrock, M. Cai, B. Liaw, Y. S. Meng, *Nat. Energy* **2021**, *6*, 987.
[24] T. Wei, Z.-H. Zhang, Z.-M. Wang, Q. Zhang, Y. Ye, J.-H. Lu, Z. Rahman, Z.-W. Zhang, *ACS Appl. Energy Mater.* **2020**, *3*, 9428.
[25] Z. Li, H.-M. Huang, J.-K. Zhu, J.-F. Wu, H. Yang, L. Wei, X. Guo, *ACS Appl. Mater. Interfaces* **2019**, *11*, 784.
[26] L. Chen, Y. Li, S.-P. Li, L.-Z. Fan, C.-W. Nan, *J. B. Goodenough, Nano Energy* **2018**, *46*, 176.
[27] C.-Z. Zhao, X.-Q. Zhang, X.-B. Cheng, R. Zhang, R. Xu, P.-Y. Chen, H.-J. Peng, J.-Q. Huang, Q. Zhang, *Proc. Natl. Acad. Sci. USA* **2017**, *114*, 11069.
[28] J. Xiong, W. Zhang, Y. Song, K. Wen, Y. Zhou, G. Chen, *L. Zhu, Appl. Sci.* **2023**, *13*, 4161.
[29] J. A. Guemes, J. M. Menéndez, *Compos. Sci. Technol.* **2002**, *62*, 959.
[30] R. Gafsi, M. A. El-Sherif, *Opt. Fiber Technol.* **2000**, *6*, 299.
[31] C.-J. Bae, A. Manandhar, P. Kiesel, A. Raghavan, *Energy Technol.* **2016**, *4*, 851.
[32] O. Yoji, Y. Shigeki, K. Tatsuro, T. Nobuo, *Smart Mater. Struct.* **2000**, *9*, 832.
[33] X. Hu, Z. Zhang, X. Zhang, Y. Wang, X. Yang, X. Wang, M. Fayena-Greenstein, H. A. Yehezkel, S. Langford, D. Zhou, B. Li, G. Wang, D. Aurbach, *Nat. Rev. Mater.* **2024**, *9*, 305.
[34] Y. Li, X. Feng, G. Yang, W. Y. Lieu, L. Fu, C. Zhang, Z. Xing, M.-F. Ng, Q. Zhang, W. Liu, J. Lu, Z. W. Seh, *Nat. Commun.* **2024**, *15*, 9364.
[35] C. D. Fincher, C. E. Athanasiou, C. Gilgenbach, M. Wang, B. W. Sheldon, W. C. Carter, Y.-M. Chiang, *Joule* **2022**, *6*, 2794.
[36] G. Li, Z. Han, Y. Tan, Q. Wei, E. Mao, J. Du, L. Fu, *Electrochim. Acta* **2024**, *473*, 143504.
[37] J. Gao, C. Chen, Q. Dong, J. Dai, Y. Yao, T. Li, A. Rundlett, R. Wang, C. Wang, L. Hu, *Adv. Mater.* **2021**, *33*, 2005305.
[38] C.-H. Zhang, Y.-J. Guo, S.-J. Tan, Y.-H. Wang, J.-C. Guo, Y.-F. Tian, X.-S. Zhang, B.-Z. Liu, S. Xin, J. Zhang, L.-J. Wan, Y.-G. Guo, *Sci. Adv.* **2024**, *10*, adl4842.
[39] L. Fu, M. Wan, B. Zhang, Y. Yuan, Y. Jin, W. Wang, X. Wang, Y. Li, L. Wang, J. Jiang, J. Lu, Y. Sun, *Adv. Mater.* **2020**, *32*, 2000952.
[40] H. Li, T. Yamaguchi, S. Matsumoto, H. Hoshikawa, T. Kumagai, N. L. Okamoto, T. Ichitsubo, *Nat. Commun.* **2020**, *11*, 1584.
[41] S. Luo, Z. Wang, X. Li, X. Liu, H. Wang, W. Ma, L. Zhang, L. Zhu, X. Zhang, *Nat. Commun. 2021 12*, 6968.
[42] L. L. Baranowski, C. M. Heveran, V. L. Ferguson, C. R. Stoldt, *ACS Appl. Mater. Interfaces* **2016**, *8*, 29573.
[43] Y. He, M. Zhang, A. Wang, B. Zhang, H. Pham, Q. Hu, L. Sheng, H. Xu, L. Wang, J. Park, X. He, *ACS Appl. Mater. Interfaces* **2022**, *14*, 33952.
[44] X. Wang, Y. He, S. Tu, L. Fu, Z. Chen, S. Liu, Z. Cai, L. Wang, X. He, Y. Sun, *Energy Storage Mater.* **2022**, *49*, 135.
[45] B. Hennequart, M. Platonova, R. Chometon, T. Marchandier, A. Benedetto, E. Quemin, R. Dugas, C. Lethien, J.-M. Tarascon, *ACS Energy Lett.* **2024**, *9*, 454.
[46] X. Gao, B. Liu, B. Hu, Z. Ning, D. S. Jolly, S. Zhang, J. Perera, J. Bu, J. Liu, C. Doerrer, E. Darnbrough, D. Armstrong, P. S. Grant, P. G. Bruce, *Joule* **2022**, *6*, 636.
[47] T. Y. Kwon, K. T. Kim, D. Y. Oh, Y. B. Song, S. Jun, Y. S. Jung, *Energy Storage Mater.* **2022**, *49*, 219.
[48] J.-M. Doux, H. Nguyen, D. H. S. Tan, A. Banerjee, X. Wang, E. A. Wu, C. Jo, H. Yang, Y. S. Meng, *Adv. Energy Mater.* **2020**, *10*, 1903253.
[49] K. T. Kim, T. Y. Kwon, Y. B. Song, S.-M. Kim, S. C. Byun, H.-S. Min, S. H. Kim, Y. S. Jung, *Chem. Eng. J.* **2022**, *450*, 138047.
[50] J. Qu, J. Xiao, T. Wang, D. Legut, Q. Zhang, *J. Phys. Chem. C* **2020**, *124*, 24644.